

Research Article

A Novel Waveform Design Method for Shift-Frequency Jamming Confirmation

Chang Zhou ¹, Zhen-Bo Zhu,² and Zi-Yue Tang²

¹The Graduate Management Group, Air Force Early Warning Academy, Huangpu Avenue, Wuhan, China

²The First Department, Air Force Early Warning Academy, Huangpu Avenue, Wuhan, China

Correspondence should be addressed to Chang Zhou; zc_radar@sohu.com

Received 31 January 2018; Accepted 19 April 2018; Published 2 July 2018

Academic Editor: Pierfrancesco Lombardo

Copyright © 2018 Chang Zhou et al. This is an open access article distributed under the Creative Commons Attribution License, which permits unrestricted use, distribution, and reproduction in any medium, provided the original work is properly cited.

Shift-frequency jamming is generally used to form range false targets for ground-based early-warning radar systems; the frequency shift value of such interference is larger than the Doppler shift value of the moving target, and the key element to suppress the shift-frequency jamming is the frequency shift value estimation. However, in the low- or medium-pulse repetition frequency (PRF) mode, it is challenging to estimate the accurate frequency shift due to the velocity ambiguity. To solve this problem, a novel sparse Doppler-sensitive waveform is designed based on the ambiguity function theory, where the basic idea is to design a waveform sensitive to a specific Doppler but insensitive to other Dopplers; therefore, this waveform can recognize the specific Doppler of the target unambiguously. To apply the designed waveform in practice, the detection and estimation processing flow is provided based on the waveform diversity technique and the family of the sparse Doppler-sensitive waveforms. Simulation experiments are presented to validate the efficiency of the proposed method, and we conclude that the advantage of this method is that it can be used to confirm the specific Doppler of the target unambiguously with few pulses even under the condition of a low PRF.

1. Introduction

Linear frequency-modulated (LFM) signals are widely used in radar systems due to their large time-bandwidth product and large Doppler tolerance [1]. Taking advantage of the range-Doppler coupling characters of LFM signals, shift-frequency jamming [2, 3] has been extensively studied, as this approach can form false targets ahead of true targets by adjusting the parameters of the frequency shift even if the radar adopts the working mode of the frequency agility or pulse repetition frequency (PRF) agility. Since the frequency shift modulation of the jammer is similar to the Doppler modulation of the moving target, it is even more challenging to recognize shift-frequency jamming. However, the frequency shift amount of the jamming is much larger than the Doppler of the moving target in ground-based early-warning radar. For example, when the L-band radar operating wavelength $\lambda \geq 15$ cm, the speed of a conventional aircraft is less than Mach (Ma) 3; thus, the Doppler frequency is less than 5.4 kHz, while the L-band signal bandwidth is

several MHz. To form a false target with at least one range cell offset, the minimum frequency shift should be many tens of kHz, which can be considered much larger than the Doppler of moving targets. Therefore, accurate estimation of the frequency shift amount or Doppler frequency can enable shift-frequency interference recognition and suppression in ground-based early-warning radar. However, for low- and medium-PRF radars, it is challenging to obtain the actual Doppler because of the velocity ambiguity. To address this challenge, the PRF agility technology is typically used for velocity ambiguity resolution [1] in practice, while the existing ambiguity resolution algorithm has the following shortcomings [4, 5]: (1) the algorithm requires a relatively high Doppler resolution in each PRF even in the presence of noise pollution and quantization errors, (2) the maximum unambiguous Doppler improvement is limited, and (3) the computation complexity is expensive, particularly in the case of multiple moving targets. Therefore, this study attempts to achieve the frequency shift estimation from the perspective of waveform design.

Many waveform design studies have focused on the low autocorrelation sidelobe [6–10], which can improve the detection performance for weak targets. The research hotspots have developed from the design of binary-phase sequences to polyphase sequences and from fixed-length sequences to arbitrary-length sequences. In recent years, related algorithms can produce unimodular sequences of the length $N = 10^6$ or even longer, with favourable autocorrelation properties [8]. In addition, several new applications, such as the sparse frequency waveform [11, 12], weighted sidelobe waveform [8], and orthogonal signal [6], have been developed. The autocorrelation of the waveform is equivalent to the zero-Doppler cut of the ambiguity function [13]; despite the fact that a satisfactory autocorrelation sidelobe waveform cannot guarantee the detection performance of moving targets, the design methods can be easily generalized for a proper ambiguity function cut design.

To detect a moving target, other possible Doppler cuts of the ambiguity function must be considered. In other words, we must consider the ambiguity function for a nonzero Doppler. The studies of [14–16] focused on synthesizing an arbitrary desired ambiguity function. Although extensive work has been performed, there is no universal method to solve this problem because it is challenging to determine whether the desired ambiguity function can be synthesized; in addition, the process is time-consuming.

Therefore, to reduce complexity, some scholars have relied on satisfying the partial constraints, such as ensuring a clear area near the origin [6] and minimizing the integral sidelobe level (ISL) in a certain area [17]. More specifically, the output response in certain range-Doppler areas, which cover the interferences, should be as small as possible, whereas the output response in certain range-Doppler areas with targets must ensure a level that is as high as possible [18]. In [19–21], the authors addressed the waveform design in the presence of coloured Gaussian disturbance noise and solved the problem through semidefinite relaxation to achieve the optimal detection performance. For the unknown Doppler, an algorithm to guarantee that the minimum Doppler matches the output maximum has been proposed [22, 23], but the signal bandwidth and ISL were not considered. The unimodular quadratic programme (UQP) and computational approaches to tackle the UQP were summarized in [24]. In [25], the clutter model was established, and a slow-time ambiguity function design was performed, which is a more intuitive way to implement the moving target detection (MTD) response. This problem has also been solved based on the maximum-block-improvement (MBI) method [26], and the majorization-minimization (MM) method was used in [18] to solve this problem and obtain improved performance. However, the ambiguity design method still addresses the velocity ambiguity problem, and few references consider the bandwidth of the coding signal, which further limits the application in radar.

In the present study, a sparse Doppler-sensitive waveform is designed that can be used to confirm the specific Doppler of the target unambiguously. By designing a different waveform with a different specific Doppler to confirm

the different target Doppler, the large shift-frequency interference can be identified and suppressed.

The remainder of this paper is organized as follows. Section 2 presents the problem statement. Section 3 examines the signal spectrum based on the optimal detection criterion for a specific Doppler, and the waveform design algorithm is discussed. Subsequently, the method of Doppler confirmation processing is proposed based on the designed waveform in Section 4. The simulation experiments are presented in Section 5. Finally, Section 6 presents the conclusions.

2. Problem Statement

The ambiguity function is the most intuitive description of the signal output performance for different Dopplers. To facilitate the design of the coding signal, the discrete ambiguity function is expressed as [1]

$$\begin{aligned}\chi_d(n, \xi_k) &= \sum_m x(m)x^*(m-n) \exp(j\xi_k m) \\ &= \sum_\omega X^*(\omega)X(\omega - \xi_k) \exp(j\omega n),\end{aligned}\quad (1)$$

where n denotes the discrete delay series, ξ_k is the discrete Doppler frequency, $x(m)$ is the discrete coded signal, and $X(\omega)$ represents the discrete Fourier transform (DFT) of $x(m)$.

With regard to the zero-Doppler cut $\chi(\tau, 0)$ of N arbitrary complex coded signals, the maximum value is N and maximum position is $\chi(0, 0)$. For the other Doppler cuts, however, the shape is unknown. Assuming that the specific Doppler is ξ_K , to design a waveform that is sensitive to a specific Doppler but insensitive to the others, the ambiguity figure must satisfy three shape constraints, as shown in Figure 1.

- (1) The specific Doppler cut (when $\xi_k = \xi_K$) should exist as a clear peak value $\chi(q, \xi_K)$ as the mainlobe, where $q \in [-(N-1), -(N-2), \dots, (N-1)]$ represents the position of the mainlobe (peak value) in this cut, and this cut can be set according to the actual requirements.
- (2) The sidelobe of the specific Doppler cut (when $\xi_k = \xi_K$ and $n \neq q$) should be as small as possible.
- (3) Other Doppler cuts (when $\xi_k \neq \xi_K$ and $\xi_k \neq \xi_0$) should not have significant peak values.

3. Proposed Method of Waveform Design

Based on the shape constraints for the ambiguity function of the sparse Doppler-sensitive waveform described in Section 2, the detailed waveform design method is discussed in this part. In Section 3.1, the sidelobe characteristics of the specific Doppler cut are analysed, and the relationship between the sidelobe of the ambiguity figure cut and the signal spectrum is deduced. Section 3.2 further builds the overall spectrum representation of the specific Doppler cut, and the signal spectrum is solved under the optimal detection criterion for the specific Doppler cut. In the end, combining the deduced

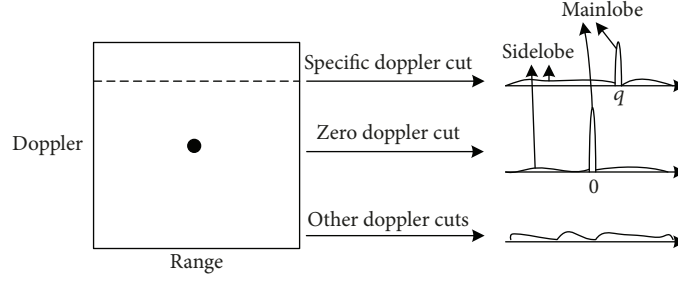


FIGURE 1: Shape constraints of various Doppler cuts in the ambiguity figure.

signal spectrum with the other Doppler cut constraints, the constant modulus waveform is designed in Section 3.3.

3.1. Analysis of the Sidelobe Characteristics of the Specific Doppler Cut (When $\xi_k = \xi_K$). It is customary to discuss the sidelobe when describing the correlation properties of the waveform. For a specific ξ_K , the discrete ambiguity function cut $\chi_d(n, \xi_K)$ is equivalent to the cross-correlation [27] of $x(n) \exp(j\xi_K n)$ and $x(n)$, which is generally expressed as $r(n, \xi_K)$. To conform to the customary representation, we define the ISL on the specific Doppler ξ_K (where q represents the position of the mainlobe in this cut) as

$$\text{ISL}_{\xi_K} = \sum_{\substack{n=-(N-1) \\ n \neq q}}^{N-1} \chi_d^2(n, \xi_K) = \sum_{\substack{n=-(N-1) \\ n \neq q}}^{N-1} r^2(n, \xi_K). \quad (2)$$

It can be verified that

$$\text{ISL}_{\xi_K} = \frac{1}{2N} \sum_{p=1}^{2N} \left[\sum_{n=-(N-1)}^{N-1} r(n, \xi_K) \exp(-j\omega_p n) - L \exp(-j\omega_p q) \right]^2 - [r(q, \xi_K) - L]^2, \quad (3)$$

where L is a complex number. Detailed derivations are given in Appendix A.

Since L could be an arbitrary complex number, to simplify the above formula, let $L = r(q, \xi_K)$; substituting this term into (3) leads to

$$\text{ISL}_{\xi_K} = \frac{1}{2N} \sum_{p=1}^{2N} \left[\sum_{n=-(N-1)}^{N-1} r(n, \xi_K) \exp(-j\omega_p n) - r(q, \xi_K) \exp(-j\omega_p q) \right]^2. \quad (4)$$

For example, if $\xi_K = 0$, $q = 0$, and $L = r(q, \xi_K) = N$, then

$$\text{ISL}_{\xi_K} = \frac{1}{2N} \sum_{p=1}^{2N} \left[\sum_{n=-(N-1)}^{N-1} r(n, 0) \exp(-j\omega_p n) - N \right]^2. \quad (5)$$

Equation (5) has been widely used to design the autocorrelation waveform [8] with low ISL. The derivation of this article has relatively extensive adaptability.

According to the relationship between the power spectrum and cross-correlation function, the following equation holds, and more derivations are obtained in Appendix B.

$$\begin{aligned} & \sum_{n=-(N-1)}^{N-1} r(n, \xi_K) \exp(-j\omega_p n) \\ &= \sum_{m=1}^N x(m) \exp(j\xi_K m) \exp(-j\omega_p m) \\ & \cdot \left(\sum_{m=1}^N x(m) \exp(-j\omega_p m) \right)^*, \end{aligned} \quad (6)$$

where $\omega_p = (2\pi/2N) \cdot p$, $p = 1, 2, \dots, 2N$, and $\xi_K = (2\pi/N) \cdot K$, $K = 1, \dots, N$.

Define $X_{\text{zerofill}}(\omega_p) = \sum_{m=1}^N x(m) \exp(-j\omega_p m)$; then, (6) can be expressed as

$$\sum_{n=-(N-1)}^{N-1} r(n, \xi_K) \exp(-j\omega_p n) = X_{\text{zerofill}}(\omega_p - \xi_K) X_{\text{zerofill}}^*(\omega_p). \quad (7)$$

Substituting (7) into (4), we obtain

$$\text{ISL}_{\xi_K} = \frac{1}{2N} \sum_{p=1}^{2N} \left[X_{\text{zerofill}}(\omega_p - \xi_K) X_{\text{zerofill}}^*(\omega_p) - r(q, \xi_K) \exp(-j\omega_p q) \right]^2. \quad (8)$$

Equation (8) is applicable to any ambiguity figure cut $\chi_d(n, \xi_K)$, which is also the basis of the following deduction.

3.2. Analysis of the Signal Spectrum under the Optimal Detection Criterion for the Specific Doppler Cut (When $\xi_k = \xi_K$). The purpose of the waveform design is to achieve effective detection. To improve the detection performance of the specific Doppler ξ_K , we need to ensure that (1) $\chi_d(q, \xi_K)$ is as large as possible and (2) ISL_{ξ_K} should be as small as possible.

Notably, since $X_{\text{zerofill}}(\omega_p) = \sum_{m=1}^N x(m) \exp(-j\omega_p m)$, $X_{\text{zerofill}}(\omega_p)$ is the DFT of $[x(1), x(2), \dots, x(N), \underbrace{0, \dots, 0}_N]$.

After adding zeros, the shape of the ambiguity figure remains the same, and according to Parseval's theorem, we can obtain

$$\begin{aligned}\chi_d(q, \xi_K) &= r(q, \xi_K) = \sum_{p=1}^N X^*(\omega_p) X(\omega_p - \xi_K) \exp(j\omega_p q) \\ &= \frac{1}{2} \cdot \sum_{p=1}^{2N} X_{\text{zerofill}}^*(\omega_p) X_{\text{zerofill}}(\omega_p - \xi_K) \exp(j\omega_p q).\end{aligned}\quad (9)$$

From (8) and (9), we find that the key to design the sparse Doppler-sensitive waveform for the specific Doppler ξ_K is $X_{\text{zerofill}}(\omega_p - \xi_K) X_{\text{zerofill}}^*(\omega_p)$. For the convenience of calculation, the complex envelope of $X_{\text{zerofill}}(\omega_p - \xi_K) X_{\text{zerofill}}^*(\omega_p)$ is designated A_{ω_p, ξ_K} , and the phase is θ_{ω_p, ξ_K} , that is, $X_{\text{zerofill}}(\omega_p - \xi_K) X_{\text{zerofill}}^*(\omega_p) = A_{\omega_p, \xi_K} \exp(j\theta_{\omega_p, \xi_K})$. Simultaneously, the complex envelope of $X_{\text{zerofill}}(\omega_p)$ is designated A_{ω_p} and the phase is θ_{ω_p} , that is, $X_{\text{zerofill}}(\omega_p) = A_{\omega_p} \exp(j\theta_{\omega_p})$; clearly, $A_{\omega_p, \xi_K} \geq 0$ and $A_{\omega_p} \geq 0$.

To fully characterize the signal spectrum after the Doppler shift, the bandwidth of the designed signal B is chosen as half of the sampling frequency f_s . Thus, the signal spectrum does not alias after the frequency shift. If the total point number is $2N$, we suppose that $A_{\omega_p} = 0$ for $p = N + 1, \dots, 2N$ in this study.

Therefore, the objective function to obtain the optimal detecting performance for the Doppler ξ_K is

$$\begin{aligned}\max \quad & P_1(A_{\omega_p, \xi_K}, \theta_{\omega_p, \xi_K}) = |\chi_d(q, \xi_K)|^2 \\ &= \left[\sum_{p=1}^{2N} A_{\omega_p, \xi_K} \exp(j\theta_{\omega_p, \xi_K}) \exp(j\omega_p q) \right]^2, \\ \min \quad & P_2(A_{\omega_p, \xi_K}, \theta_{\omega_p, \xi_K}) = \text{ISL}_{\xi_K} \\ &= \frac{1}{2N} \sum_{p=1}^{2N} \left[A_{\omega_p, \xi_K} \exp(j\theta_{\omega_p, \xi_K}) \right. \\ &\quad \left. - \frac{1}{2} \left(\sum_{\bar{p}=1}^{2N} A_{\omega_{\bar{p}}, \xi_K} \exp(j\theta_{\omega_{\bar{p}}, \xi_K}) \exp(j\omega_{\bar{p}} q) \right) \right. \\ &\quad \left. \cdot \exp(-j\omega_p q) \right]^2, \\ \text{s.t.} \quad & \theta_{\omega_p, \xi_K} = \theta_{\omega_{p-K}} - \theta_{\omega_p}, A_{\omega_p, \xi_K} \\ &= A_{\omega_p} \cdot A_{\omega_{p-K}} |A_{\omega_p}| = 0, \quad p = N + 1, \dots, 2N, \\ & \sum_{p=1}^{2N} |A_{\omega_p}|^2 = N^2.\end{aligned}\quad (10)$$

Equation (10) is a nonlinear biobjective function for which it is challenging to obtain an analytic solution. First, we adopt the method of weighted sums to solve the problem, and the total objective function is

$$\begin{aligned}\max \quad & P(A_{\omega_p, \xi_K}, \theta_{\omega_p, \xi_K}) = P_1(A_{\omega_p, \xi_K}, \theta_{\omega_p, \xi_K}) \\ &+ \lambda P_2(A_{\omega_p, \xi_K}, \theta_{\omega_p, \xi_K}),\end{aligned}\quad (11)$$

Requirements: sequence length N , weight coefficient λ

1. Initialize: $\theta_{\omega_p, \xi_K} = -\omega_p q$.
2. Repeat.
3. Substitute θ_{ω_p, ξ_K} to the total objective function (12).
4. Compute A_{ω_p} through sequential quadratic programming.
5. Compute A_{ω_p, ξ_K} according to $A_{\omega_p, \xi_K} = A_{\omega_p} \cdot A_{\omega_{p-K}}$.
6. Compute θ_{ω_p, ξ_K} using the genetic algorithm.
7. Continue until convergence.

ALGORITHM 1: Signal spectrum under the condition of optimal detection criteria for a specific Doppler ξ_K .

where λ is the weight coefficient and the constraints remain the same. In (11), P_1 's weight should be large because if no target of the specific Doppler can be detected results from the low detection probability, even the lowest sidelobe is useless.

Then, we design the θ_{ω_p, ξ_K} and A_{ω_p} separately using the iterative algorithm for the optimal solution. When A_{ω_p} is fixed, then A_{ω_p, ξ_K} is fixed according to $A_{\omega_p, \xi_K} = A_{\omega_p} \cdot A_{\omega_{p-K}}$, and a genetic algorithm [28] is employed to quantify the phase and identify the optimal θ_{ω_p, ξ_K} . While θ_{ω_p, ξ_K} is fixed, the function degenerates to a real optimization problem with nonlinear multiconstraints, and this problem can be solved through sequential quadratic programming [29]. If MATLAB (a commercial mathematics software produced by American MathWorks company) is available, then A_{ω_p} can be solved using the MATLAB function "fmincon" [30].

The iterative algorithm is described as follows.

3.3. Waveform Design Method. After discussing the signal spectrum for the specific Doppler ξ_K in Section 3.2, two further steps are required to complete the design of the signal: (1) designing the constant modulus waveform approaching the signal spectrum and (2) establishing the constraints necessary to avoid other Doppler cuts existing at significant peak values.

From Section 3.2, for the given specific Doppler ξ_K and mainlobe position q , we obtain θ_{ω_p, ξ_K} and A_{ω_p} . While $\theta_{\omega_p, \xi_K} = \theta_{\omega_{p-K}} - \theta_{\omega_p}$ according to (11), knowledge of the first K phases is required to obtain the complete θ_{ω_p} .

For step (1), let \mathbf{F} be the unit DFT matrix as follows:

$$\mathbf{F} = \frac{1}{\sqrt{2N}} [\mathbf{f}(0) \mathbf{f}(1) \cdots \mathbf{f}(2N-1)], \quad (12)$$

where \mathbf{f} denotes the vector value functions, given by

$$\mathbf{f}(p) = \left[\exp\left(j\frac{2\pi}{2N}p \cdot 0\right) \cdots \exp\left(j\frac{2\pi}{2N}p \cdot (2N-1)\right) \right]^T, \quad (13)$$

where $(\cdot)^T$ denotes the transpose for matrices/vectors. We define the unimodular signal vector $\tilde{\mathbf{X}}$ and the discrete spectrum vector \mathbf{D} as follows:

$$\tilde{\mathbf{X}} = \begin{bmatrix} x(1) \\ x(2) \\ \vdots \\ x(N) \\ 0 \\ \vdots \\ 0 \end{bmatrix}_{2N}, \quad (14)$$

$$\mathbf{D} = \begin{bmatrix} X(\omega_1) \\ X(\omega_2) \\ \vdots \\ \vdots \\ X(\omega_{2N}) \end{bmatrix} = \begin{bmatrix} A_{\omega_1} \exp(j\theta_{\omega_1}) \\ A_{\omega_2} \exp(j\theta_{\omega_2}) \\ \vdots \\ \vdots \\ A_{\omega_{2N}} \exp(j\theta_{\omega_{2N}}) \end{bmatrix}.$$

The optimal spectral constraint problem is

$$\begin{aligned} \min \quad & P(\tilde{\mathbf{X}}, \mathbf{D}) = \|\mathbf{F}^H \tilde{\mathbf{X}} - \mathbf{D}\|^2, \\ \text{s.t.} \quad & |x(n)| = 1, \quad n = 1, 2, \dots, N, \\ \exp \quad & \left(j\theta_{\omega_p} \right) \exp \left(-j\theta_{\omega_{p-K}} \right) = \exp \left(j\theta_{\omega_p, \xi_K} \right), \\ & p = K + 1, \dots, N, \end{aligned} \quad (15)$$

where $(\cdot)^H$ and $\|\cdot\|$ denote the conjugate transpose and Frobenius norm for matrices/vectors, respectively.

For step (2), to realize the other Dopplers' insensitivity, since the other Doppler cuts can be regarded as the sidelobe of the entire ambiguity figure, the multicyclic original (multi-CAO) algorithm [6], which is typically used to minimize the discrete ambiguity figure sidelobe of the partial interested area, is introduced to design the signal.

Define vector $\mathbf{X} = [\mathbf{X}_1 \cdots \mathbf{X}_P]_{(N+Q-1) \times Q(K-1)}$, where Q is the number of interested range cell number and K is the specific Doppler:

$$\mathbf{X}_m = \begin{bmatrix} x_m(1) & & 0 \\ \vdots & \ddots & \\ \vdots & & x_m(1) \\ x_m(N) & \vdots & \\ & \ddots & \vdots \\ 0 & & x_m(N) \end{bmatrix}_{(N+Q-1) \times Q}, \quad m = 1, 2, \dots, K-1, \quad (16)$$

where $x_m(n) = x(n)e^{j2\pi(n(m-1)/N)}$, $m = 1, 2, \dots, K-1$, and $n = 1, 2, \dots, N$. The number of Doppler cells of interest is $K-1$. The algorithm is described in detail elsewhere [6]. The sidelobe constraint is

$$\begin{aligned} \min \quad & P(\mathbf{X}, \mathbf{U}) = \|\mathbf{X} - \sqrt{N}\mathbf{U}\|^2, \\ \text{s.t.} \quad & |x(n)| = 1, \quad n = 1, 2, \dots, N, \\ & \mathbf{U}^H \mathbf{U} = \mathbf{I}. \end{aligned} \quad (17)$$

Adding (15) and (17) with their corresponding weights, the total objective function is

$$\begin{aligned} \min \quad & P(\tilde{\mathbf{X}}, \mathbf{X}, \mathbf{U}, \mathbf{D}) = \|\mathbf{F}^H \tilde{\mathbf{X}} - \mathbf{D}\|^2 + \eta \|\mathbf{X} - \sqrt{N}\mathbf{U}\|^2, \\ \text{s.t.} \quad & |x(n)| = 1, \quad n = 1, 2, \dots, N, \\ \exp \quad & \left(j\theta_{\omega_p} \right) \exp \left(-j\theta_{\omega_{p-K}} \right) \\ & = \exp \left(j\theta_{\omega_p, \xi_K} \right), \quad p = K + 1, \dots, N, \\ & \mathbf{U}^H \mathbf{U} = \mathbf{I}, \end{aligned} \quad (18)$$

where η is the weight coefficient.

The waveform design algorithm is described as follows.

4. Application Method of the Specific Doppler Confirmation

4.1. Waveform Property and Performance Evaluation. To enable quantitative analysis of the designed waveform property, we consider the main characteristics of the waveform. In Section 3.2, the objective function P_1 is configured with a larger weight since a high peak value level for the specific Doppler cut should be guaranteed to ensure the matched filter output level; thus, the properties of the optimal signal solution of P_1 can represent the main characteristics of the waveform. The optimal solution of P_1 is $\theta_{\omega_p, \xi_K} = -\omega_p q$, which can be written as $\exp(j\theta_{\omega_p}) \exp(-j\theta_{\omega_{p-K}}) = \exp(j\omega_p q)$; letting $A_{\omega_p} = 1$, the properties of the waveform are discussed as follows:

- (1) If the maximum position is q for the specific Doppler ξ_K , then $|\chi_d(q, \xi_K)|$ is the maximum value for this Doppler cut. Under this condition, we can derive that $|\chi_d(lq, \xi_{lK})|$ is also the maximum value for the Doppler ξ_{lK} , where l denotes any positive integer. More details are given in Appendix C.
- (2) The possible maximum in the ambiguity figure may appear in (n, k) , which satisfies the formula $Kn - kq = \pm d \cdot 2N$, which can be easily proven using f_3 and f_4 in Appendix D. Figure 2 displays the shape of f_1 , f_2 , f_3 , and f_4 in Appendix D, where $N = 50$, $K = 5$, $q = 1$, and the first K phases of the frequency are random. The conclusion can also be observed from Figure 1.
- (3) For all points (n, k) satisfying $Kn - kq = \pm d \cdot 2N$, the amplitude $|\chi_d(q, \xi_K)|$ is modulated by the first K phases, and the different first K phases may lead to different ambiguity figures. Figure 3 shows the ambiguity function (D.5) in Appendix D, where $N = 50$, $K = 5$, and $q = 1$. Figures 3(a) and 3(b) show the case

Requirements: sequence length N , weight coefficient η

1. Initialize: $\{x(n)\}_{n=1}^N$ is a randomly generated unimodular sequence; configure $\tilde{\mathbf{X}}$ and \mathbf{X} .

2. Repeat.

3. For a fixed $\tilde{\mathbf{X}}$, compute the first K complex values of θ_{ω_p} according to $\theta_{\omega_p, \xi_K} = \theta_{\omega_p, K} - \theta_{\omega_p}$ and $\mathbf{F}^H \tilde{\mathbf{X}} - \mathbf{D}$.

4. For a fixed \mathbf{X} , the minimizer \mathbf{U} is given by $\mathbf{U} = \mathbf{U}_2 \mathbf{U}_1^H$, where matrices \mathbf{U}_1 and \mathbf{U}_2 are taken from the economic SVD of \mathbf{X}^H , which is $\mathbf{X}^H = \mathbf{U}_1 \Sigma \mathbf{U}_2^H$.

5. For a fixed \mathbf{D} , $x(n) = \exp(j \arg(\mathbf{f}^T(n) \mathbf{D}))$.

6. For a fixed \mathbf{U} , the criterion can be written as

$$\|\mathbf{X} - \sqrt{N} \mathbf{U}\|^2 = \sum_{n=1}^N \sum_{l=1}^{(K-1)Q} |\mu_{nl} x(n) - v_{nl}|^2 = \text{const} - 2 \sum_{n=1}^N \text{Re} \left[\left(\sum_{l=1}^{(K-1)Q} \mu_{nl}^* v_{nl} \right) x^*(n) \right],$$

where const is a constant that does not depend on $\{x(n)\}$; $\{\mu_{nl}\}$ are given by the elements of \mathbf{X} that contain $x(n)$

$$[\mu_{n1} \cdots \mu_{n, (K-1)Q}] = \left[\underbrace{1 \cdots 1}_{K-1} \underbrace{e^{j2\pi(n/N)} \cdots e^{j2\pi(n/N)}}_{K-1} \cdots \underbrace{e^{j2\pi(n(Q-1)/N)} \cdots e^{j2\pi(n(Q-1)/N)}}_{K-1} \right]_{1 \times (K-1)Q}$$

$\{v_{nl}\}$ are the elements of $\sqrt{N} \mathbf{U}$, whose positions are identical to those of $\{\mu_{nl}\}$ in \mathbf{X} . The minimizer $x(n)$ is

$$x(n) = \exp \left(j \arg \left(\sum_{l=1}^{(K-1)Q} \mu_{nl}^* v_{nl} \right) \right), \quad n = 1, \dots, 2N.$$

7. Summarize the results in step 5 and step 6; the minimizer $x(n)$ is given by

$$x(n) = \exp \left(j \arg \left\{ \eta (\mathbf{f}^T \mathbf{D}) + (1 - \eta) \left(\sum_{l=1}^{(K-1)Q} \mu_{nl}^* v_{nl} \right) \right\} \right).$$

8. Continue until convergence.

ALGORITHM 2: Sparse Doppler-sensitive waveform design algorithm with a constant modulus constraint.

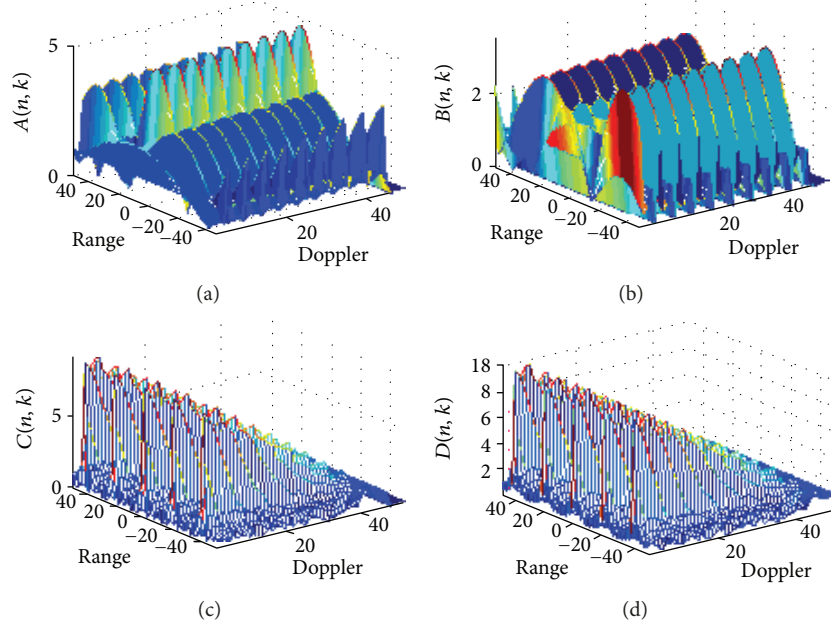


FIGURE 2: f_1, f_2, f_3 , and f_4 in Appendix D ($N = 50$, and the first K phases of the frequency are random).

in which the first K phases of the frequency are random, whereas Figures 3(c) and 3(d) show the case in which the first K phases of the frequency are equal. Thus, the results vary significantly according to the first K phases of the frequency.

In addition, Figures 3(c) and 3(d) are similar to the LFM signal, which can be explained by the fact that the LFM can be considered a form of designed signal in this study, where $K = 1$ and $q = 2$. In contrast, if K is sufficiently large, then the designed waveform becomes a random sequence phase

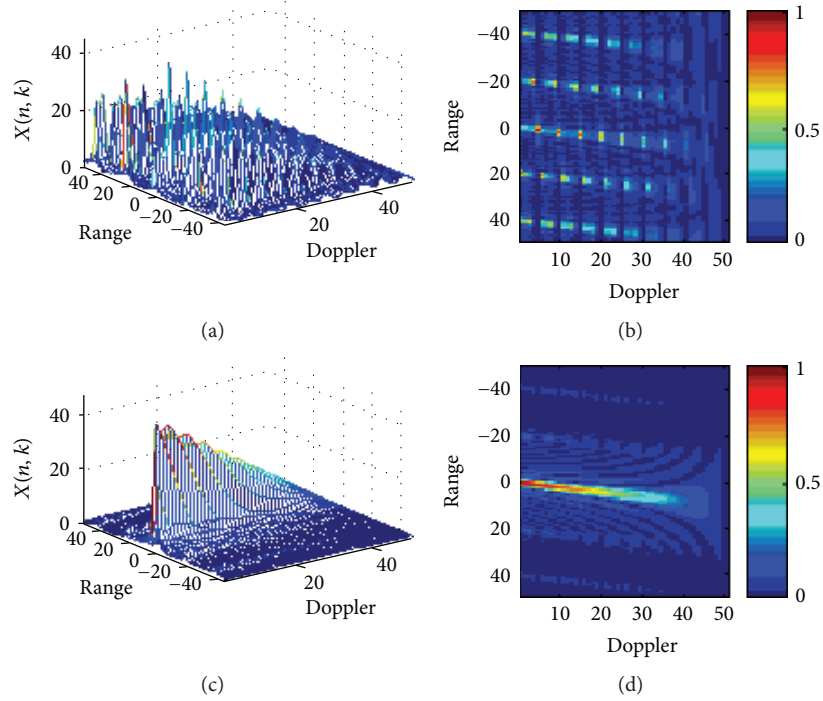


FIGURE 3: Ambiguity function ($N = 50$). (a, b) The first K phases of the frequency are random; (c, d) the first K phases of the frequency are equal.

encoding signal with an “acicular” ambiguity figure. In summary, the sparse Doppler-sensitive waveform is a waveform family that includes the LFM signal and random sequence phase encoding signal.

In this section, we also discuss the Doppler resolution Δf of the technique. Suppose that the signal bandwidth is B , the sampling frequency is f_s , and the time duration is T in each pulse repetition period. The number of sampling points is N , where $N = T/f_s$; therefore, $\Delta f = f_s/N = f_s/(T \cdot f_s) = 1/T$. The maximum unambiguous Doppler increases from the pulse repetition frequency f_r to the sampling frequency f_s ; thus, this parameter can be used to recognize the large shift-frequency interference.

4.2. Application Method of Waveform Diversity for Auxiliary Doppler Confirmation. Due to its inherent cyclicity, which is discussed in depth in Section 4.1, the designed signal cannot be directly used in signal detection on its own. Thus, the signal here is combined with the LFM signal to measure the specific Doppler target simultaneously, as shown in the flow chart of the proposed application technique in Figure 4. In this technique, two types of radar working modes are given: normal mode and measuring mode.

In normal mode, the LFM signal is used to detect the target individually in the same manner as other regular radar measurements. When the specific Doppler ξ_K requires confirmation, the signal can be switched to measuring mode. In this mode, the LFM signal and signals I and II with parameters (N, B, K, q_1) and (N, B, K, q_2) , respectively, are transmitted in order, where N and B are the sampling points and bandwidth of the transmitting pulse, respectively, which can be identical to the LFM to confuse the enemy jammer. K

depends on the specific Doppler ξ_K , and q_1 and q_2 denote the maximum position of Doppler ξ_K cut for signal I and signal II, respectively. P_{f1} denotes the constant false alarm rate (CFAR) of transmitting the LFM signal, and P_{f2} is the CFAR of transmitting signal I and signal II.

For a specific Doppler ξ_K , q_1 determines the relative position of the target of Doppler ξ_K between the LFM signal and signal I. Similarly, q_2 determines the relative position of the target of Doppler ξ_K between the LFM signal and signal II. If the received signals from the transmitting signals (i.e., the LFM signal and signals I and II) satisfy the relative range offset for the specific Doppler ξ_K , then the Doppler of the target can be confirmed as ξ_K . In short, this technique confirms the Doppler by comparing the range offsets of various waveforms.

Further, the reason to use two additional signals to complete the measurement is that the sidelobe of the designed waveform is larger than the LFM signal; thus, P_{f2} is made to be relatively large to ensure high detection probability, and the overall false alarm can be reduced through the joint detection.

5. Numerical Experiments

Example 1. There are three targets; the Doppler of the true target 1 is 20 kHz, the Doppler of false target 2 and false target 3 is 30 kHz and 40 kHz (generated by shift-frequency jamming), respectively, the wavelength is $\lambda = 0.1$ m, and the signal-to-noise ratio (SNR) of all the targets is -5 dB before pulse compression. For the LFM signal and signals I and II, the bandwidth is 1 MHz, the time width is $100 \mu\text{s}$,

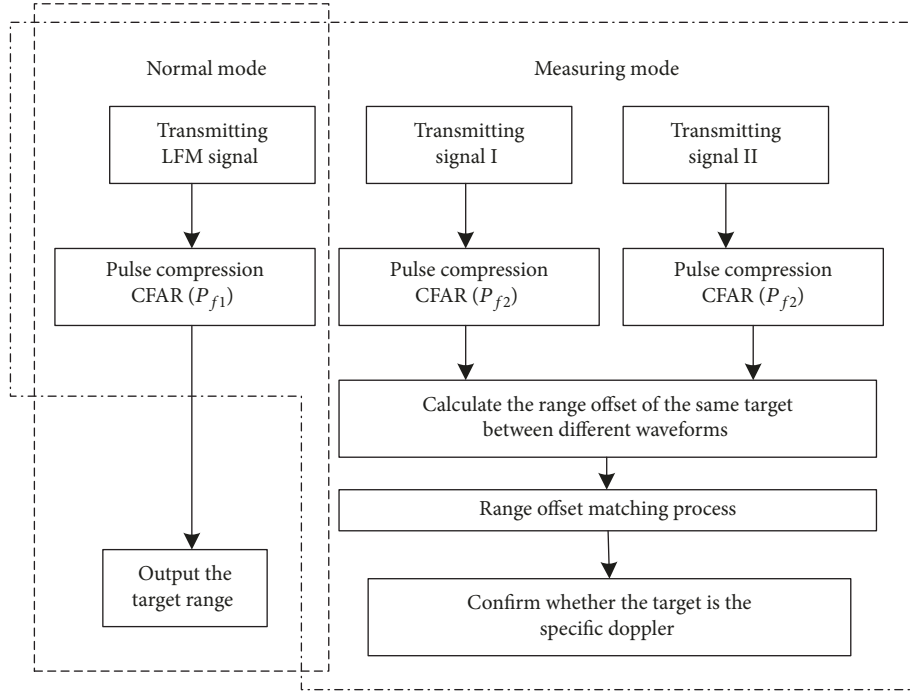


FIGURE 4: Flow chart of the proposed application technique.

TABLE 1: Signal parameters and target positions (in theory).

Signal (parameter)	Target 1 range (range cell)	Target 2 range (range cell)	Target 3 range (range cell)
LFM signal	1.02×10^{-4} s (204)	1.105×10^{-4} s (221)	1.215×10^{-4} s (243)
Signal I ($K = 3, q_1 = 2$)	None	1.085×10^{-4} s (217)	None
Signal II ($K = 3, q_2 = 3$)	None	1.09×10^{-4} s (218)	None

and the sampling frequency is 2 MHz. To measure different Dopplers, we set different K and q values to match different Dopplers based on Section 5. The square law detection is used with $P_{f1} = 10^{-6}$ and $P_{f2} = 10^{-3}$. Signal parameters and the corresponding target positions in theory are shown in Table 1. Figures 5 and 6 show the ambiguity figure of the sparse Doppler-sensitive waveform with the parameters set to $K = 3$ and $q_1 = 2$. Figure 5 shows that when the Doppler number is 1 or 2, the ambiguity cut has no significant peak output, whereas when the Doppler number is 3, corresponding to a waveform design parameter of $K = 3$, the ambiguity cut has a prominent mainlobe and relatively low sidelobe. In addition, the multiple Doppler number of 3 also has a peak output, which is displayed in Figure 6; the results prove the conclusion derived in Section 4.1, and the graph can fully represent the sparsity of the waveform.

Clearly, the speed of a normal aircraft is less than Ma 3, and the Doppler should be less than 20.4 kHz; thus, targets 2 and 3 must be false targets. While MTD processing is used, the Doppler of signals 2 and 3 ranges from zero to several hundred Hz due to the velocity ambiguity (the

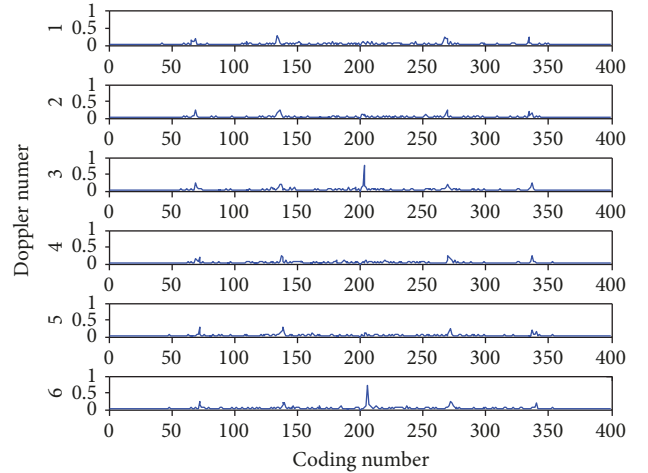


FIGURE 5: Ambiguity figure cut of Doppler numbers 1 to 6.

PRF of early-warning radar is typically 200–500 Hz), and the false targets cannot be effectively identified. Therefore, a correct measurement is the key to recognize large shift-frequency interference.

Figure 7 shows the received results of transmitting the LFM signal and signals I and II after pulse compression for three targets. The relative range offsets between LFM, signal I, and signal II for all targets are consistent with Table 1. When transmitting signal I and signal II with $K = 3$, only target 2 displays a peak output response since the specific Doppler is 30 kHz in this case. In addition, the designed signal (signals I and II) has a higher sidelobe than the LFM signal. Consequently, the detection performance is worse than that of the LFM signal.

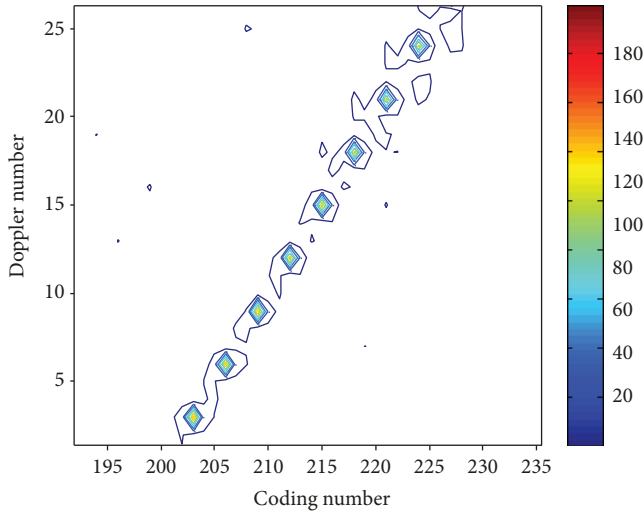


FIGURE 6: Contour map of the ambiguity figure.

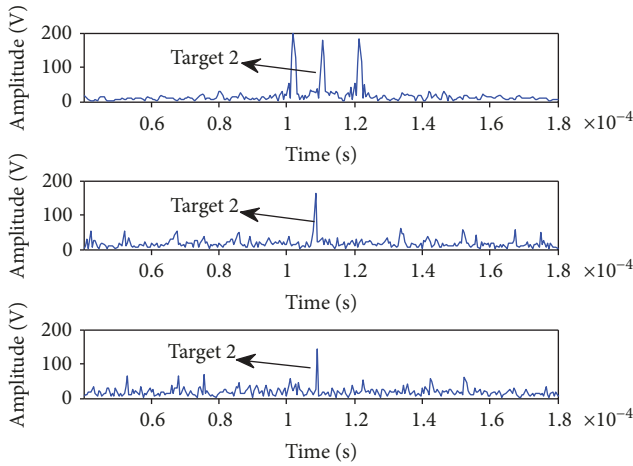


FIGURE 7: Results of transmitting the LFM signal, signal I ($K = 3, q_1 = 2$) and signal II ($K = 3, q_2 = 3$) after the pulse compression.

Figure 8 represents the received results of transmitting the LFM and signals I and II after CFAR detection. In Figure 8, the range offset between the different waveforms for target 2 corresponds to the theoretical offset of the specific Doppler at 30 kHz, and the Doppler of target 2 can be determined to be 30 kHz. Although a high P_{f_2} may cause false alarm points when transmitting signal I and signal II individually, the entire CFAR can remain at a relatively low level since the correct confirming results require joint offset detection matching, which means that the target must be detected in the corresponding positions of three figures simultaneously, which is challenging for any false alarm points.

In addition, the simulation results also show one advantage of the method relative to PRF agility: if the SNR is sufficient to allow detection, then the confirmation can be performed with notably few pulses.

Example 2. In this simulation, we analyse the robustness of the method. The parameter setting is identical to that of

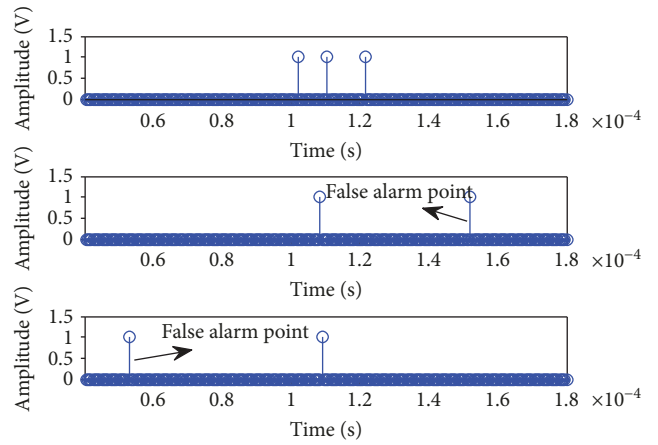


FIGURE 8: Results of transmitting the LFM signal and signal I ($K = 3, q_1 = 2$) and signal II ($K = 3, q_2 = 3$) after CFAR (square law detection).

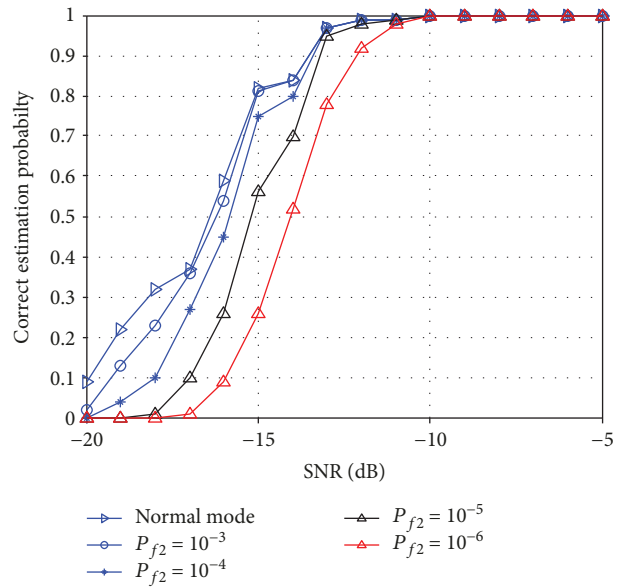


FIGURE 9: Probability of correct confirmation for target 2.

Example 1, and the results are obtained using 1×10^6 Monte Carlo runs.

Figure 9 shows the probability of correct confirmation versus the SNR of the targets before pulse compression; the results correspond to target 2. The probability of correct confirmation indicates that the likelihood of target 2 being accurately confirmed is 30 kHz. The normal mode is set as a reference group that represents the probability of target 2 being detected by the LFM signal.

The curves in Figure 9 highlight that the probability increases when the SNR increases, while the probability decreases when P_{f_2} decreases. When P_{f_2} is relatively large, such as 10^{-3} , the correct confirmation probability is nearly equal to the detection probability of the normal mode, which means that the target can be correctly confirmed as long as the target can be detected by the LFM signal. When the

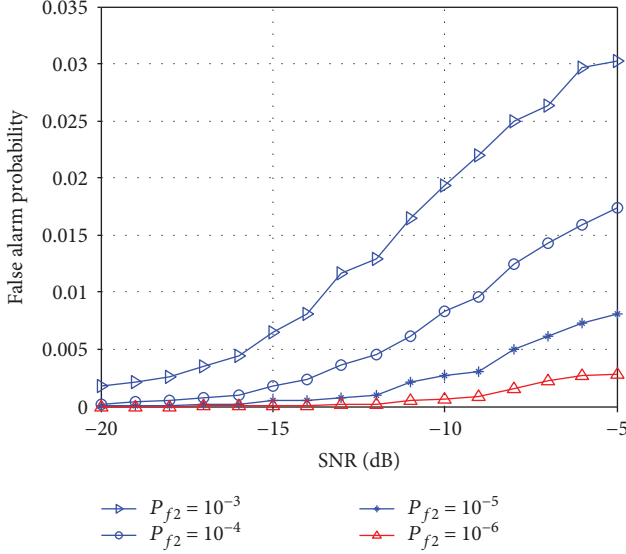


FIGURE 10: Probability of false alarm detection (signal I).

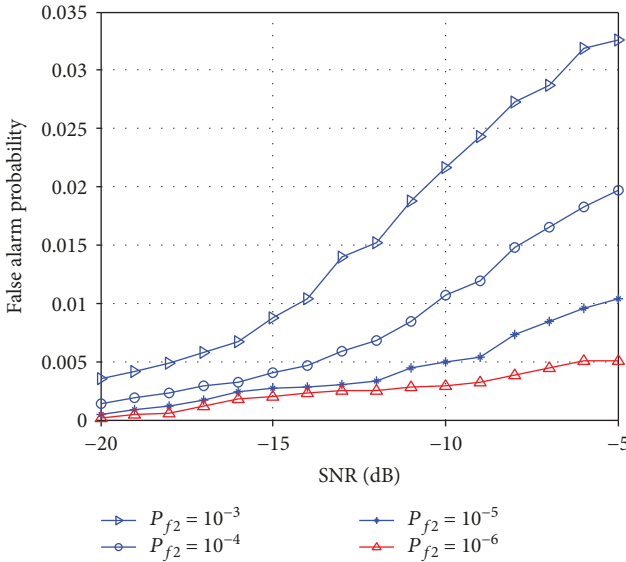


FIGURE 11: Probability of false alarm detection (signal II).

SNR before pulse compression is larger than -10 dB, the correct estimation probability approaches 1, demonstrating that the performance of the algorithm is robust even in the case of low P_{f_2} . However, the performance varies substantially if the SNR is less than -10 dB; for example, when the SNR is equal to -15 dB, the probability difference between $P_{f_2} = 10^{-3}$ and $P_{f_2} = 10^{-6}$ is predicted to be 0.5. Thus, we conclude that P_{f_2} should be larger when the SNR is relatively low.

The results of Figures 10 and 11 also show the false alarm probability of signal I and signal II, respectively, versus the SNR of the targets before pulse compression. Since P_{f_2} represents only the false alarm probability in the case of noise, the sidelobe of the designed waveform also affects the false alarm probability.

The false alarm probability is relatively high for a single waveform, and the curves highlight that a larger SNR leads to a higher false alarm probability. Although the waveform diversity technology is exploited to reduce the overall false alarm probability through joint detection, it is preferred to adopt smaller P_{f_2} when the SNR is large (such as $\text{SNR} > -10$ dB) since this condition may cause false judgement of other target results from the false alarm points.

6. Conclusion

In this study, we investigated the problem of shift-frequency interference with radar, where the Doppler shift value estimation is the key for antijamming techniques, and a method for specific Doppler confirmation processing is provided from the perspective of the waveform. The main contributions of this study are summarized as follows:

- (i) The relationship between the ISL of an arbitrary Doppler ambiguity figure cut and the signal spectrum is derived.
- (ii) The optimal signal spectrum based on the optimal detection criterion for a specific Doppler is obtained.
- (iii) A sparse Doppler-sensitive waveform sensitive to a specific Doppler but insensitive to other Dopplers is designed.
- (iv) The application method of waveform diversity for the specific Doppler confirmation in the fast-time domain is proposed based on the designed waveform.

In addition, the Doppler number of the true targets is relatively small in ground-based early-warning radar, and we need not address the excessive spending of radar detection resources to confirm much Doppler information using this method. Furthermore, the ratio of jamming to noise (JNR) is always sufficient to detect, and the confirmation can be performed with notably few pulses relative to the PRF agility.

Appendix

A.

Proof. Equation (3) holds due to

$$\begin{aligned}
 & \sum_{p=1}^{2N} \left[\sum_{n=-(N-1)}^{N-1} r(n, \xi_K) \exp(-j\omega_p n) - L \exp(-j\omega_p q) \right]^2 \\
 &= \sum_{p=1}^{2N} \left[\sum_{n=-(N-1)}^{N-1} r(n, \xi_K) \exp(-j\omega_p n) \right. \\
 &\quad \left. - \sum_{n=-(N-1)}^{N-1} L \delta_{n-q} \exp[-j\omega_p(n-q)] \exp(-j\omega_p n) \right]^2 \\
 &= \sum_{p=1}^{2N} \left[\sum_{n=-(N-1)}^{N-1} [r(n, \xi_K) - L \delta_{n-q}] \exp(-j\omega_p n) \right]^2
 \end{aligned}$$

$$\begin{aligned}
&= 2N \cdot \sum_{n=-(N-1)}^{N-1} [r(n, \xi_K) - L\delta_{n-q}]^2 \\
&= 2N \cdot \left[\sum_{\substack{n=-(N-1) \\ n \neq q}}^{N-1} r^2(n, \xi_K) + [r(q, \xi_K) - L]^2 \right] \\
&= 2N \cdot [\text{ISL}_{\xi_K} + [r(q, \xi_K) - L]^2],
\end{aligned} \tag{A.1}$$

where δ_K is the Kronecker delta:

$$\delta_K = \begin{cases} 1, & \text{for } K = 0, \\ 0, & \text{for } K \neq 0. \end{cases} \tag{A.2}$$

Extracting the ISL_{ξ_K} to the left of the equation, we find that (3) is valid.

B.

Proof. Equation (6) holds due to

$$\begin{aligned}
&\sum_{m=1}^N x(m) \exp(j\xi_K m) \exp(-j\omega_p m) \cdot \left(\sum_{m=1}^N x(m) \exp(-j\omega_p m) \right)^* \\
&= \sum_{m=1}^N x(m) \exp(j\xi_K m) \exp(-j\omega_p m) \sum_{m=1}^N x^*(m) \exp(j\omega_p m) \\
&= \sum_{m=1}^N \sum_{\tilde{m}=1}^N x(m) \exp(j\xi_K m) \exp(-j\omega_p m) x^*(\tilde{m}) \exp(j\omega_p \tilde{m}) \\
&= \sum_{m=1}^N \sum_{\tilde{m}=1}^N [x(m)x^*(\tilde{m}) \exp(j\xi_K m)] \cdot \exp[-j\omega_p(m - \tilde{m})].
\end{aligned} \tag{B.1}$$

Let $m - \tilde{m} = n$, we can obtain

$$\begin{aligned}
&\sum_{m=1}^N \sum_{\tilde{m}=1}^N [x(m)x^*(\tilde{m}) \exp(j\xi_K m)] \cdot \exp[-j\omega_p(m - \tilde{m})] \\
&= \sum_{n=-(N-1)}^{N-1} r(n, \xi_K) \exp(-j\omega_p n).
\end{aligned} \tag{B.2}$$

C.

Proof. This part discusses the periodicity of the signal. The phase of the signal spectral $X(\omega_p)$ is defined as $\angle X(\omega_p)$, where $p = 1, 2, \dots, 2N$. If the given condition is $X(\omega_p - \xi_K)$ $X^*(\omega_p) = A_{\omega_p, \xi_K} \exp(-j\omega_p q + j\varphi)$, then

$$\begin{aligned}
\angle X(\omega_p) &= \angle X(\omega_{p-K}) \exp(j\omega_p q - j\varphi) \\
&= \angle X(\omega_{p-2K}) \exp(j\omega_{p-2K} q - j\varphi) \exp(j\omega_p q - j\varphi) \\
&= \angle X(\omega_{p-lK}) \exp(j\omega_{p-(K-1)} q - j\varphi) \cdots \exp(j\omega_p q - j\varphi) \\
&= \angle X(\omega_{p-lK}) \exp(j\omega_p l q) \exp\left(-j \frac{2\pi(l-1)Klq}{2N} - jK\varphi\right),
\end{aligned} \tag{C.1}$$

where l and K are given; $\exp(-j(2\pi/2N)((l-1)Klq/2) - jK\varphi)$, is a fixed value, and we can obtain

$$\begin{aligned}
X(\omega_p - \xi_{lK}) X^*(\omega_p) &= A_{\omega_p, \xi_{lK}} \exp(-j\omega_p l q) \exp \\
&\cdot \left(-j \frac{2\pi(l-1)Klq}{2N} - jK\varphi \right).
\end{aligned} \tag{C.2}$$

Although $A_{\omega_p, \xi_{lK}}$ is not known, for $\chi_d(n, \xi_{lK}) = \sum_{p=1}^{2N} X^*(\omega_p) X(\omega_p - \xi_{lK}) \exp(j\omega_p n)$, the maximum value must be $\chi_d(lq, \xi_{lK})$.

D.

Proof. In this part, we derive the ambiguity function section of another Doppler k when Doppler K is configured. Since $p = 1, 2, \dots, 2N$, we can write $p = i + lK$, where $i = 1, 2, \dots, K$ and $l = 0, 1, \dots, \lceil 2N/K \rceil - 1$; thus,

$$\begin{aligned}
\angle X(\omega_p) &= \angle X(\omega_{i+lK}) = \angle X(\omega_{i+(l-1)K}) \exp(j\omega_{i+lK} q - j\varphi) \\
&= \angle X(\omega_{i+(l-2)K}) \exp(j\omega_{i+(l-1)K} q - j\varphi) \exp(j\omega_{i+lK} q - j\varphi) \\
&= \angle X(\omega_i) \exp(j\omega_{i+K} q - j\varphi) \cdots \exp(j\omega_{i+lK} q - j\varphi) \\
&= \angle X(\omega_i) \exp\left(j \frac{2\pi}{2N} \cdot \frac{2i + K + lK}{2} \cdot lq\right) \exp(-jl\varphi).
\end{aligned} \tag{D.1}$$

Then, we must obtain the value of $\angle X(\omega_p - \xi_k)$. Let $k = j + mK$, where $j = 1, 2, \dots, K$ and $m = 0, 1, \dots, \lceil 2N/K \rceil - 1$. Since the bandwidth of the signal is half of the sampling frequency,

$$\begin{aligned}
&\sum_{p=1}^{2N} X^*(\omega_p) X(\omega_p - \xi_k) \exp(j\omega_p n) \\
&= \sum_{p=1}^N X^*(\omega_p) X(\omega_p - \xi_k) \exp(j\omega_p n).
\end{aligned} \tag{D.2}$$

According to the symmetrical characteristic, considering only the case of $i + lK > j + mK$, we discuss the cases of $i > j$, $l \geq m$ and $i \leq j$, $l > m$ separately.

(1) When $i > j$, $l \geq m$

$$\begin{aligned}
\angle X(\omega_p - \xi_k) &= \angle X(\omega_{(i-j)+(l-m)K}) \\
&= \angle X(\omega_{i-j}) \exp \\
&\quad \cdot \left(j \frac{2\pi}{2N} \frac{2(i-j) + (l-m+1)K}{2} (l-m)q \right) \\
&\quad \cdot \exp(-j(l-m)\varphi).
\end{aligned} \tag{D.3}$$

(2) When $i \leq j, l > m$

$$\begin{aligned}
\angle X(\omega_p - \xi_k) &= \angle X(\omega_{(i-j+K)+(l-m-1)K}) \\
&= \angle X(\omega_{i-j+K}) \exp \\
&\quad \cdot \left(j \frac{2\pi}{2N} \frac{2(i-j+K) + (l-m)K}{2} (l-m-1)q \right) \\
&\quad \cdot \exp(-j(l-m-1)\varphi).
\end{aligned} \tag{D.4}$$

The ambiguity function is as follows:

$$\begin{aligned}
&\sum_{p=k+1}^N X^*(\omega_p) X(\omega_p - \xi_k) \exp(j\omega_p n) \\
&= \sum_{i=1}^j \sum_{l=m+1}^{\lceil 2N/K \rceil - 1} \angle X^*(\omega_i) \exp\left(-j \frac{2\pi}{2N} \cdot \frac{2i+K+lK}{2} \cdot lq\right) \\
&\quad \cdot \exp(jl\varphi) \angle X(\omega_{i-j+K}) \cdot \exp \\
&\quad \cdot \left(j \frac{2\pi}{2N} \frac{2(i-j+K) + (l-m)K}{2} (l-m-1)q \right) \\
&\quad \cdot \exp(-j(l-m-1)\varphi) \exp(j\omega_p n) + \sum_{i=j+1}^K \sum_{l=m}^{\lceil 2N/K \rceil - 1} \angle X^*(\omega_i) \\
&\quad \cdot \exp\left(-j \frac{2\pi}{2N} \cdot \frac{2i+K+lK}{2} \cdot lq\right) \exp(jl\varphi) \angle X(\omega_{i-j}) \\
&\quad \cdot \exp\left(j \frac{2\pi}{2N} \frac{2(i-j) + (l-m+1)K}{2} (l-m)q \right) \\
&\quad \cdot \exp(-j(l-m)\varphi) \exp(j\omega_p n) = \sum_{i=1}^j \angle X^*(\omega_i) \angle X(\omega_{i-j+K}) \\
&\quad \cdot \exp\left(j \frac{2\pi}{2N} \frac{(2i-2j+2K-mK)(-m-1)}{2} q \right) \\
&\quad \cdot \exp\left(j \frac{2\pi}{2N} \text{in} \right) \exp(j(m+1)\varphi) \sum_{l=m+1}^{\lceil 2N/K \rceil - 1} \exp \\
&\quad \cdot \left(j \frac{2\pi}{2N} (Kn - (j+mK)q)l \right) + \sum_{i=j+1}^K \angle X^*(\omega_i) \angle X(\omega_{i-j}) \\
&\quad \cdot \exp\left(j \frac{2\pi}{2N} \frac{-2mi+2mj+Km^2-Km}{2} q \right)
\end{aligned}$$

$$\begin{aligned}
&\cdot \exp\left(j \frac{2\pi}{2N} \text{in} \right) \exp(jm\varphi) \sum_{l=m}^{\lceil 2N/K \rceil - 1} \exp \\
&\quad \cdot \left(j \frac{2\pi}{2N} (Kn - (j+mK)q)l \right) = f_1 \sum_{l=m+1}^{\lceil 2N/K \rceil - 1} \exp \\
&\quad \cdot \left(j \frac{2\pi}{2N} (Kn - kq)l \right) + f_2 \sum_{l=m}^{\lceil 2N/K \rceil - 1} \exp\left(j \frac{2\pi}{2N} (Kn - kq)l \right) \\
&= f_1 \cdot f_3 + f_2 \cdot f_4.
\end{aligned} \tag{D.5}$$

where

$$\begin{aligned}
f_1 &= \sum_{i=1}^j \angle X^*(\omega_i) \angle X(\omega_{i-j+K}) \\
&\quad \cdot \exp\left(j \frac{2\pi}{2N} \frac{(2i-2j+2K-mK)(-m-1)}{2} q \right) \\
&\quad \cdot \exp\left(j \frac{2\pi}{2N} \text{in} \right) \exp(j(m+1)\varphi), \\
f_2 &= \sum_{i=j+1}^K \angle X^*(\omega_i) \angle X(\omega_{i-j}) \\
&\quad \cdot \exp\left(j \frac{2\pi}{2N} \frac{-2mi+2mj+Km^2-Km}{2} q \right) \\
&\quad \cdot \exp\left(j \frac{2\pi}{2N} \text{in} \right) \exp(jm\varphi), \\
f_3 &= \sum_{l=m+1}^{\lceil 2N/K \rceil - 1} \exp\left(j \frac{2\pi}{2N} (Kn - (j+mK)q)l \right), \\
f_4 &= \sum_{l=m}^{\lceil 2N/K \rceil - 1} \exp\left(j \frac{2\pi}{2N} (Kn - (j+mK)q)l \right).
\end{aligned} \tag{D.6}$$

Data Availability

All data are provided in full in this paper.

Conflicts of Interest

The authors declare that there are no conflicts of interest regarding the publication of this paper.

Acknowledgments

This work was partially supported by a grant from the National Natural Science Foundation of China (61671469).

References

- [1] M. A. Richards, *Fundamentals of Radar Signal Processing*, McGraw-Hill, New York, NY, USA, 2nd edition, 2014.
- [2] K. L. Wei, N. Tai, L. Huang, and N. C. Yuan, "Shift-frequency jamming against pulse compression radar," in *2016 Progress in*

- Electromagnetic Research Symposium (PIERS)*, pp. 2251–2254, Shanghai, China, August 2016.
- [3] C. P. Huang, J. Wang, and B. G. Xu, “Performance of shift-frequency jamming against LFM signal pulse,” *Systems engineering and Electronics*, vol. 35, no. 5, pp. 935–939, 2013.
 - [4] J. Sun, J. Tian, and G. Wang, “Doppler ambiguity resolution for multiple PRF radar using iterative adaptive approach,” *Electronics Letters*, vol. 46, no. 23, pp. 1562–1563, 2010.
 - [5] M. Y. Xia, W. M. Su, H. Gu, and J. C. Lu, “Research on velocity ambiguity resolution for multiple PRF radar,” *Journal of Electronics & Information technology*, vol. 39, no. 12, pp. 2860–2865, 2017.
 - [6] H. He, J. Li, and P. Stoica, *Waveform Design for Active Sensing Systems: a Computational Approach*, Cambridge University Press, Cambridge, 2012.
 - [7] M. Soltanalian and P. Stoica, “Designing unimodular codes via quadratic optimization,” *IEEE Transactions on Signal Processing*, vol. 62, no. 5, pp. 1221–1234, 2014.
 - [8] P. Stoica, H. He, and J. Li, “New algorithms for designing unimodular sequences with good correlation properties,” *IEEE Transactions on Signal Processing*, vol. 57, no. 4, pp. 1415–1425, 2009.
 - [9] J. X. Song, P. Badu, and D. P. Palomar, “Sequence design to minimize the weighted integrated and peak sidelobe levels,” *IEEE Transactions on Signal Processing*, vol. 64, no. 8, pp. 2051–2064, 2016.
 - [10] J. X. Song, P. Badu, and D. P. Palomar, “Optimization methods for designing sequences with low autocorrelation sidelobes,” *IEEE Transactions on Signal Processing*, vol. 63, no. 15, pp. 3998–4009, 2015.
 - [11] H. He, P. Stoica, and J. Li, “Waveform design with stopband and correlation constraints for cognitive radar,” in *2010 2nd International Workshop on Cognitive Information Processing*, pp. 344–349, Elba, Italy, June 2010.
 - [12] X. Feng, Y. C. Song, Z. Q. Zhou, and Y. N. Zhao, “Designing unimodular waveform with low range sidelobes and stopband for cognitive radar via relaxed alternating projection,” *International Journal of Antennas and Propagation*, vol. 2016, Article ID 6280508, 9 pages, 2016.
 - [13] N. Levanon and E. Mozeson, *Radar Signals*, Wiley-IEEE Press, New York, NY, USA, 2004.
 - [14] S. Sussman, “Least-square synthesis of radar ambiguity functions,” *IRE Transactions on Information Theory*, vol. 8, no. 3, pp. 246–254, 1962.
 - [15] J. D. Wolf, G. M. Lee, and C. E. Suvo, “Radar waveform synthesis by mean square optimization techniques,” *IEEE Transactions on Aerospace and Electronic Systems*, vol. AES-5, no. 4, pp. 611–619, 1969.
 - [16] A. Bonami, G. Garrigos, and P. Jaming, “Discrete radar ambiguity problems,” *Applied and Computational Harmonic Analysis*, vol. 23, no. 3, pp. 388–414, 2005.
 - [17] D. Eustice, C. Baylis, C. Latham, R. J. Marks, and L. Cohen, “Optimizing radar waveforms using generalized alternating projections,” in *2015 Texas Symposium on Wireless and Microwave Circuits and Systems (WMCS)*, pp. 1–6, Waco, TX, USA, April 2015.
 - [18] L. L. Wu, P. Babu, and P. Daniel, “Cognitive radar-based sequence design via SINR maximization,” *IEEE Transactions on Signal Processing*, vol. 65, no. 3, pp. 779–793, 2017.
 - [19] A. De Maio, S. D. Nicola, Y. Huang, Z.-Q. Luo, and S. Zhang, “Design of phase codes for radar performance optimization with a similarity constraint,” *IEEE Transactions on Signal Processing*, vol. 57, no. 2, pp. 610–621, 2009.
 - [20] A. De Maio, S. D. Nicola, Y. Huang, S. Zhang, and A. Farina, “Code design to optimize radar detection performance under accuracy and similarity constraints,” *IEEE Transactions on Signal Processing*, vol. 56, no. 11, pp. 5618–5629, 2008.
 - [21] A. De Maio, S. D. Nicola, Y. Huang, D. P. Palomar, S. Zhang, and A. Farina, “Code design for radar STAP via optimization theory,” *IEEE Transactions on Signal Processing*, vol. 58, no. 2, pp. 679–694, 2010.
 - [22] A. De Maio, Y. Huang, and M. Piezzo, “A Doppler robust max-min approach to radar code design,” *IEEE Transactions on Signal Processing*, vol. 58, no. 9, pp. 4943–4947, 2010.
 - [23] A. De Maio, Y. Huang, M. Piezzo, S. Zhang, and A. Farina, “Design of optimized radar codes with a peak to average power ratio constraint,” *IEEE Transactions on Signal Processing*, vol. 59, no. 6, pp. 2683–2697, 2011.
 - [24] M. A. Kerahroodi, A. Aubry, A. De Maio, M. M. Naghsh, and M. Modarres-Hashemi, “A Coordinate-Descent Framework to Design Low PSL/ISL Sequences,” *IEEE Transactions on Signal Processing*, vol. 65, no. 22, pp. 5942–5956, 2017.
 - [25] J. Zhang, X. Qiu, C. Shi, and Y. Wu, “Cognitive radar ambiguity function optimization for unimodular sequence,” *EURASIP Journal on Advances in Signal Processing*, vol. 2016, no. 1, 2016.
 - [26] A. Aubry, A. De Maio, B. Jiang, and S. Z. Zhang, “Ambiguity function shaping for cognitive radar via complex quartic optimization,” *IEEE Transactions on Signal Processing*, vol. 61, no. 22, pp. 5603–5619, 2013.
 - [27] R. M. Gray and J. W. Goodman, “Convolution and correlation,” in *Fourier Transforms*, vol. 322 of The Springer International Series in Engineering and Computer Science, pp. 251–307, Springer, Boston, MA, USA, 1995.
 - [28] D. E. Goldberg, *Genetic Algorithms in Search, Optimization and Machine Learning*, Addison-Wesley Pub., Massachusetts, 1989.
 - [29] R. Fletcher, S. Leyffer, and P. L. Toint, “On the global convergence of a filter-SQP algorithm,” *SIAM Journal on Optimization*, vol. 13, no. 1, pp. 44–59, 2002.
 - [30] “fmincon,” <http://www.mathworks.com/help/optim/ug/fmincon.html>.

